ACS APPLIED MATERIALS & INTERFACES

Research Article

www.acsami.org

Ultrawide Band Gap β-Ga_2O_3 Nanomechanical Resonators with Spatially Visualized Multimode Motion

Xu-Qian Zheng, Jaesung Lee, Subrina Rafique, Lu Han, Christian A. Zorman, Hongping Zhao, and Philip X.-L. Feng*

Department of Electrical Engineering & Computer Science, Case School of Engineering, Case Western Reserve University, 10900 Euclid Avenue, Cleveland, Ohio 44106, United States

Supporting Information

ABSTRACT: Beta gallium oxide (β-Ga_2O_3) is an emerging ultrawide band gap (4.5 eV–4.9 eV) semiconductor with attractive properties for future power electronics, optoelectronics, and sensors for detecting gases and ultraviolet radiation. β-Ga_2O_3 thin films made by various methods are being actively studied toward such devices. Here, we report on the experimental demonstration of single-crystal β-Ga_2O_3 nanomechanical resonators using β-Ga_2O_3 nanoflakes grown via low-pressure chemical vapor deposition (LPCVD). By investigating β-Ga_2O_3 circular drumhead structures, we demonstrate multimode nanoresonators up to the sixth mode in high and very high frequency (HF/VHF) bands, and also realize spatial mapping and visualization of the multimode motion. These measurements reveal a Young's modulus of E_Y = 261 GPa and anisotropic biaxial built-in tension of 37.5 MPa and 107.5 MPa. We find that thermal annealing can considerably improve the resonance characteristics, including ~40% upshift in frequency and ~90% enhancement in quality (Q) factor. This study lays a foundation for future exploration and development of mechanically coupled and tunable β-Ga_2O_3 electronic, optoelectronic, and physical sensing devices.

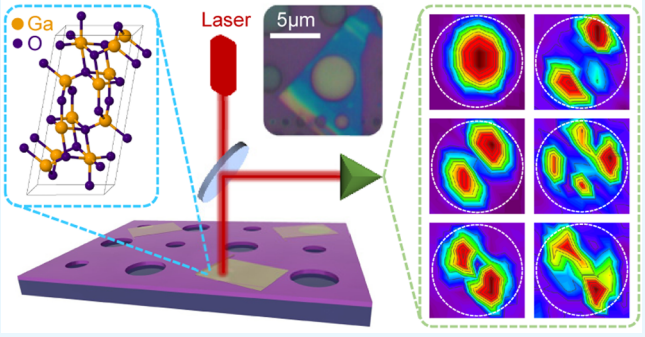

KEYWORDS: *beta gallium oxide (β-Ga_2O_3), nanoelectromechanical systems (NEMS), resonators, Young's modulus, annealing, spatial mapping, mode shape*

Wide band gap (WBG) semiconductors, such as gallium nitride (GaN) and silicon carbide (SiC), have been widely employed in power electronics and high-temperature and harsh-environment electronics and transducers, as well as in ultraviolet (UV) photonics,[1−5] thanks to their advanced material properties such as high critical field strength ($\mathcal{E}_{br,GaN} \approx$ 3.3 MV cm^{-1}, $\mathcal{E}_{br,4H\text{-}SiC} \approx$ 2.5 MV cm^{-1}) and UV photon absorption (band gap $E_{g,GaN} \approx$ 3.4 eV, $E_{g,SiC} \approx$ 2.3–3.3 eV). These WBG crystals also possess outstanding mechanical properties such as very high Young's modulus ($E_{Y,GaN} \approx$ 300 GPa, $E_{Y,SiC} \approx$ 400 GPa), exceptional thermal properties (e.g., thermal conductivity κ_{GaN} = 130 W m^{-1} K^{-1} and κ_{SiC} = 360–490 W m^{-1} K^{-1}, at ~300 K), outstanding thermal tolerance (maintaining mechanical properties up to 1300 °C), and chemical stability.[6] These characteristics, combined with readily available microfabrication techniques, make these WBG crystals technologically critical materials for advanced micro/nanoelectromechanical systems (M/NEMS) beyond the conventional counterparts based upon silicon (Si). By exploiting these advantageous properties, great progress has been made in SiC and GaN M/NEMS,[6−9] for sensing and detection of physical quantities, and in low-power signal processing at radio frequencies, especially for high-temperature and harsh-environment scenarios.

As an emerging ultrawide band gap (UWBG) semiconductor, β-Ga_2O_3 has recently attracted increasing interest because of its UWBG ($E_{g,\beta\text{-}Ga2O3} \approx$ 4.5–4.9 eV) that is significantly wider than those of GaN and SiC.[10,11] It offers very high critical field strength ($\mathcal{E}_{br,\beta\text{-}Ga2O3}$ = 8 MV cm^{-1} predicted, and $\mathcal{E}_{br,\beta\text{-}Ga2O3}$ = 3.8 MV cm^{-1} measured) and electron mobility up to μ_n = 300 cm^2 V^{-1}·s^{-1} at room temperature.[12−16] These make β-Ga_2O_3 a promising contender for future generation power devices.[15,17,18] Beyond electrical properties, β-Ga_2O_3 also exhibits excellent mechanical strength (Young's modulus $E_{Y,\beta\text{-}Ga2O3}$ = 232 GPa) along with extraordinary chemical and thermal (melting point at 1820 °C) stability.[19,20] The excellent ensemble of attributes in β-Ga_2O_3 makes it suitable for new UWBG M/NEMS beyond SiC and GaN M/NEMS. Further, β-Ga_2O_3 is sensitive to solar-blind UV light[21,22] and offers reversible response to oxidation and reduction gases,[23] enabling UV light and gas-sensing applications. Importantly, in contrast to other demonstrated WBG M/NEMS materials including SiC, diamond, and GaN, bulk β-Ga_2O_3 crystals can be made by homoepitaxy (thus preventing threading dislocations) and

Received: September 13, 2017
Accepted: November 8, 2017
Published: November 8, 2017

DOI: 10.1021/acsami.7b13930
ACS Appl. Mater. Interfaces 2017, 9, 43090–43097

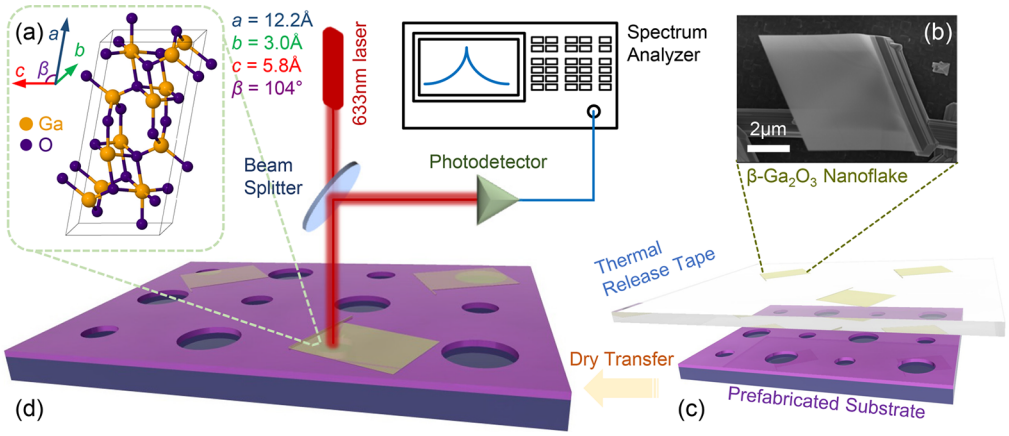

Figure 1. Schematic representation of experimental demonstration of β-Ga_2O_3 nanomechanical resonators. (a) β-Ga_2O_3 crystal structure. (b) Scanning electron microscopy (SEM) image of an as-grown β-Ga_2O_3 nanoflake extruding from a β-Ga_2O_3 nanorod grown on the 3C-SiC substrate. (c) Illustration of all-dry transfer of β-Ga_2O_3 nanoflakes by using thermal release tape as a stamp to create suspended β-Ga_2O_3 devices on predefined microtrenches and arrays. (d) Illustration of fabricated β-Ga_2O_3 resonators under study by using the scanning laser interferometry motion detection and spatial mapping system.

other more cost-effective melting growth methods, such as Czochralski (CZ),[24,25] floating zone (FZ),[26−28] and edge-defined film-fed growth (EFG)[29] techniques. The variety of synthesis methods has already led to realization of various β-Ga_2O_3 nanostructures, including nanowires,[30] nanobelts,[31] nanorods,[32] and nanosheets.[33] Given these exciting and promising properties, in parallel to currently active pursuit of electronic devices, it is intriguing to explore β-Ga_2O_3 as a new structural material for M/NEMS; it is important to gain knowledge and understanding of its mechanical properties down to the nanoscale. Toward these objectives, here we perform the first experiments on studying and exploiting mechanical properties of β-Ga_2O_3 nanoflakes by realizing the first robust β-Ga_2O_3 nanomechanical devices, from material synthesis to device fabrication and characterization. Employing all-dry-transfer techniques, we fabricate suspended β-Ga_2O_3 diaphragms based on β-Ga_2O_3 nanoflakes[34] synthesized by low-pressure chemical vapor deposition (LPCVD).[35,36] Using an ultrasensitive laser optical interferometry measurement system, we detect the undriven thermomechanical motion of these nanoresonators, from which we examine thermal annealing effects and resolve the elastic properties of the β-Ga_2O_3 nanoflakes. Further, we analyze the frequency scaling laws of multimode β-Ga_2O_3 nanoresonators and discover the anisotropic stress distribution in the β-Ga_2O_3 diaphragms by comparing finite element modeling (FEM) results with measured multimode resonances and their mode shapes.

β-Ga_2O_3 is the most stable polymorph of Ga_2O_3 which has a monoclinic crystalline structure (Figure 1a).[37] The construction of β-Ga_2O_3 suspended nanomechanical resonators starts with the synthesis of β-Ga_2O_3 nanoflakes. Using an LPCVD method,[34] we grow β-Ga_2O_3 nanostructures on a 3C-SiC epilayer on Si substrate at a growth temperature of 950 °C for 1.5 h, using high-purity Ga pellets and O_2 (Ar as carrier gas) as source materials (Figure S1 in Supporting Information (SI)). The as-grown nanoflakes have widths of ∼2−30 μm and thicknesses of ∼20−140 nm (Figure 1b). We use an all-dry-transfer method to fabricate the suspended β-Ga_2O_3 diaphragms (Figure 1c, Figure S2 in SI). The as-grown nanoflakes are picked up by thermal release tape which is then stamped onto a substrate with arrays of predefined microtrenches that are ∼290 nm deep (Figure 1c). By heating the structure to 90 °C and by gently lifting the thermal release tape, the β-Ga_2O_3 nanoflakes remain on the substrate, forming circular suspended diaphragms with diameters of ∼3.2 μm and ∼5.2 μm (set by the sizes of the prepatterned circular microtrenches). To examine the crystal quality of β-Ga_2O_3 after device fabrication, we first measure Raman spectra of the transferred flakes and find Raman modes at ∼143, ∼168, ∼199, ∼346, ∼416, ∼476, ∼653, and ∼768 cm^{-1}, excellently matching the calibrated Raman modes of bulk β-Ga_2O_3; this verifies the high crystal quality of the suspended β-Ga_2O_3 diaphragms (Figure S3 in SI).[38]

We then conduct optical resonance measurements on the β-Ga_2O_3 circular drumhead diaphragms: a He−Ne (633 nm) laser is focused upon the suspended β-Ga_2O_3 device to interferometrically detect the out-of-plane motion of the diaphragm (Figure 1d). The laser scanning interferometry detection system has been engineered to achieve[39] (1) ultrahigh displacement sensitivity (∼4 fm $Hz^{-1/2}$) in reading out flexural vibrations down to the undriven, Brownian thermomechanical motion, and (2) submicrometer-scale spatial resolution in its scanning spectromicroscopy mode, thus capable of spatially mapping and vividly visualizing the mode shapes of the multimode resonances.

We carefully investigate the multimode resonances of these devices by conducting thermal annealing at 250 °C for 1.5 h and by calibrating resonance characteristics both before and after annealing. Fundamental mode resonance spectra of a typical device with diameter d ∼ 3.2 μm (Figure 2a) before and after annealing are shown in Figure 2b and Figure 2c, respectively. Fitting the spectra to a damped simple harmonic resonator model, we find that the thermal annealing has led to a resonance frequency (f) upshift from 65.50 to 74.90 MHz and a quality (Q) factor enhancement from 420 to 566. Measured fundamental mode fs and Qs of 10 devices (Figure 2d−f) show an average f increase of ∼40% and a Q enhancement of ∼90%. The results suggest that thermal annealing (with the same parameters) may be comparatively more effective for these β-Ga_2O_3 nanoresonators than for their molybdenum disulfide (MoS_2) or hexagonal boron nitride (h-BN) counterparts (where similar thermal annealing does not cause as much measurable enhancement),[40,41] likely partially because of the relatively stronger affinity of β-Ga_2O_3 with gaseous adsorbates in ambient environment. The postannealing measured upshifts

DOI: 10.1021/acsami.7b13930
ACS Appl. Mater. Interfaces 2017, 9, 43090−43097

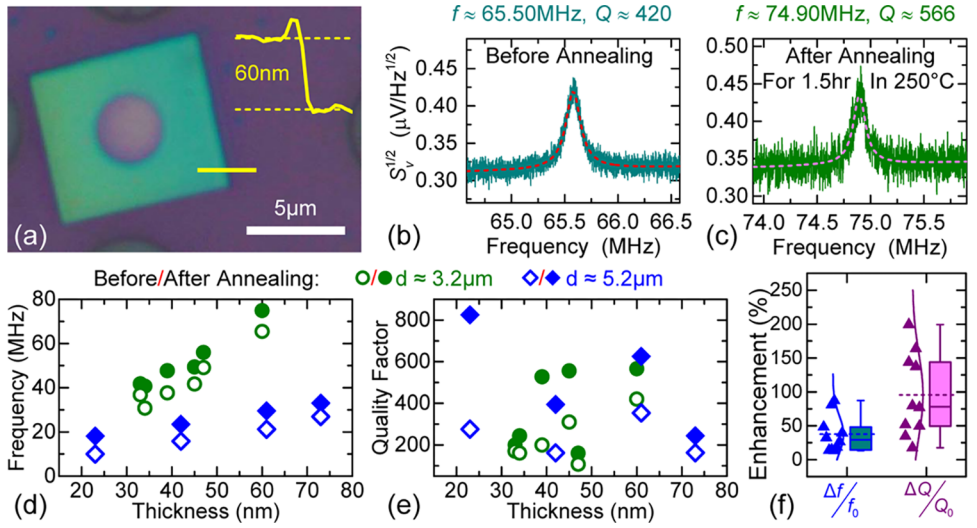

Figure 2. Measurement results of β-Ga_2O_3 diaphragm nanoresonators before and after thermal annealing. (a) Optical microscopy image of a typical β-Ga_2O_3 diaphragm nanoresonator with a diameter of $d \approx 3.2$ μm and a thickness of $t \approx 60$ nm. Inset: Atomic force microscopy (AFM) trace of the corresponding cross section labeled in the optical image. (b, c) Thermomechanical noise spectra of the device's fundamental mode, before and after a 250 °C, 1.5 h thermal annealing, respectively. (d) Fundamental mode resonance frequencies (f_0) and (e) quality (Q) factors of the β-Ga_2O_3 diaphragm nanoresonators before and after annealing. Hollow symbols show results before annealing, and solid ones show the results after annealing. Blue color diamonds represent devices with diameter $d \approx 5.2$ μm and green circles represent $d \approx 3.2$ μm devices. (f) Measured postannealing enhancement (in percentage) and dispersion of f_0 and Q.

in fs and enhanced Qs can be qualitatively explained by the annealing-enabled cleaning of possible adsorbates and residues (lowering the mass M in $\omega = \sqrt{k/M}$) and the alleviation or elimination of their associated dissipation and energy-loss processes. Most of the measured resonances show decreased dissipation rates (f/Q) after annealing (see Table S2), further confirming the alleviation of dissipation pathways by thermal annealing.

To quantitatively understand the measured resonances, we first perform analysis on multimode resonances and frequency scaling for these circular β-Ga_2O_3 diaphragms. In any given circular drumhead device, both flexural rigidity (dominated by thickness and elastic modulus) and built-in tension (stress) can be important, and thus we have[42]

$$\omega_m = (k_m a)\sqrt{\frac{D}{\rho \cdot t \cdot a^4}\left[(k_m a)^2 + \frac{\gamma \cdot a^2}{D}\right]} \quad (1)$$

where m denotes the mode number, $\omega_m = 2\pi f_m$ is the mth mode angular resonance frequency, $(k_m a)^2$ is the eigenvalue which can be numerically calculated ($k_0 a = 10.215$, $k_1 a = 21.260$, $k_2 a = 34.877$, $k_3 a = 39.771$),[42] a is the radius of circular resonator, D is the flexural rigidity $D = E_Y t^3/[12(1-\nu^2)]$ with t being the thickness of the device, ν is the Poisson's ratio, ρ is the volume mass density of β-Ga_2O_3, and γ is the surface pretension evenly distributed in the plane. Equation 1 yields a "mixed elasticity" model that captures both the "disk" and "membrane" limits of frequency scaling for such devices as well as the transition between these two regimes.[43] In the disk regime where resonance frequency is dominated by the flexural rigidity, a large D makes the $\gamma a^2/D$ term in eq 1 negligible. The resonance frequencies are positively dependent on resonator thickness, $\omega_m \propto t$. In the membrane regime where the built-in tension dominates, the term $\gamma a^2/D \gg (k_m a)^2$ and the term $(k_m a)^2$ can be neglected. The resonance frequencies scale with resonator thickness as $\omega_m \propto t^{-1/2}$. For circular drumhead resonators in the disk regime, the built-in tension has negligible effect on determining the resonance frequency. Therefore, if the device is in the disk regime, the Young's modulus can be revealed from measured fundamental-mode resonance frequency ω_0 by

$$E_Y = \frac{12a^4\rho(1-\nu^2)}{[(k_0 a)^2]^2 \cdot t^2}\omega_0^2 \quad (2)$$

with $(k_0 a)^2 = 10.215$ for the fundamental mode. We choose the applicable devices for Young's modulus extraction. By fitting and plotting the measured data to the $\omega_0 \propto t$ relation (straight dimmed solid lines in Figure 3a), we can compare the measured

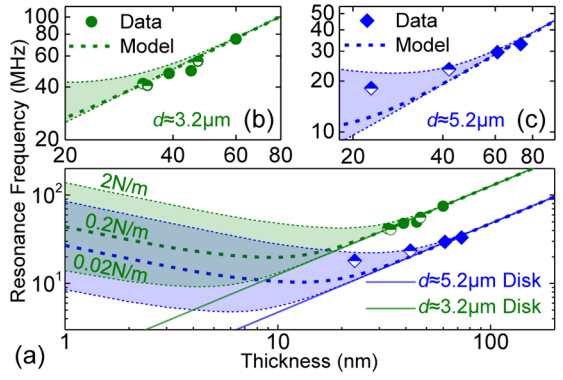

Figure 3. Modeling and elucidating the mixed elastic behavior and transition from the disk regime to the membrane regime in β-Ga_2O_3 diaphragm nanoresonators. Green circles and blue diamonds represent devices with diameters of $d \approx 3.2$ μm and $d \approx 5.2$ μm, respectively. Scattered symbols represent experimental data from optical interferometry measurements with solid ones representing devices used for Young's modulus extraction. Curved lines show calculated resonance frequency vs device thickness, each with 0.02, 0.2, and 2 N m^{-1} surface tensions, plotted using eq 1. Dimmed solid lines indicate the relation for ideal disk resonators. (a) Frequency scaling of β-Ga_2O_3 diaphragm nanoresonators with thicknesses in 1−100 nm range. (b, c) Zoomed-in scaling of measured devices' thickness ranges for resonators with diameters of $d \approx 3.2$ μm and $d \approx 5.2$ μm, respectively.

DOI: 10.1021/acsami.7b13930
ACS Appl. Mater. Interfaces 2017, 9, 43090−43097

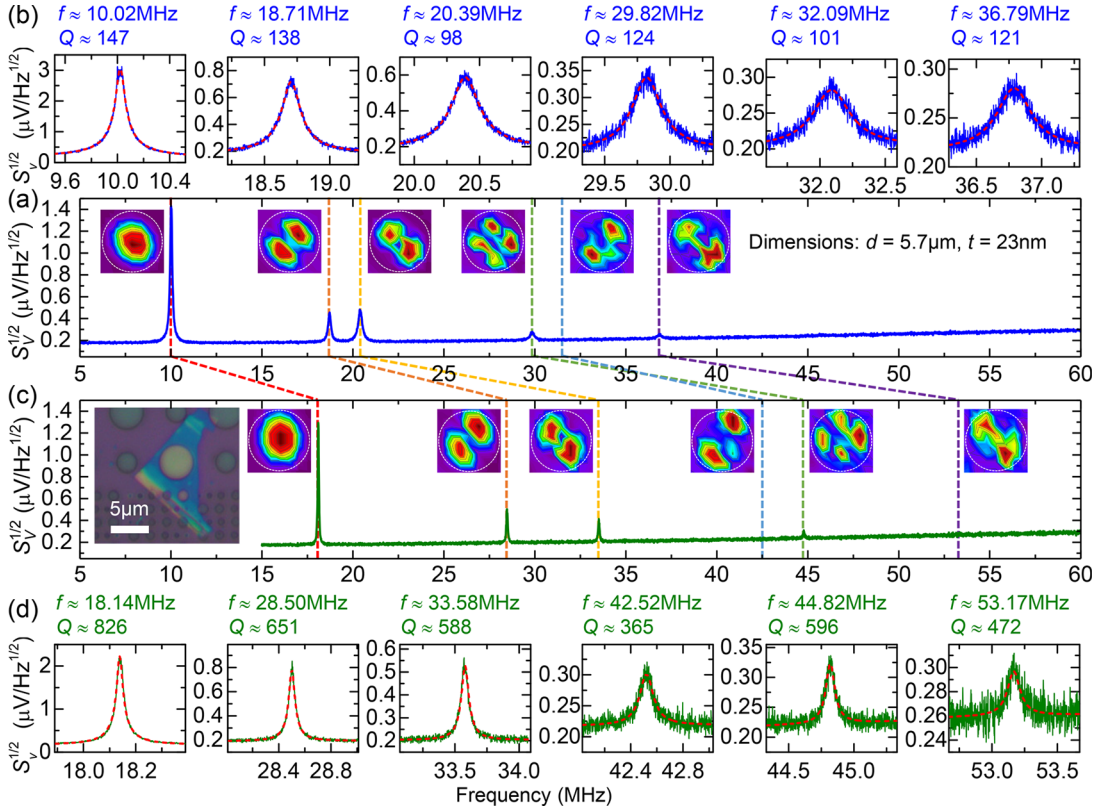

Figure 4. Comparison of measured multimode resonances before and after thermal annealing of a β-Ga_2O_3 diaphragm nanoresonator (device optical image shown in the inset of panel (c). Thermomechanical resonance spectra of (a) before and (c) after thermal annealing (250 °C, 1.5 h) with zoomed-in individual resonance spectra with fitted *f*s and *Q*s (panels in (b) and (d), respectively) and spatial mapping and visualization of the resonance mode shapes (insets of (a) and (c)).

resonance data with the ideal disk curve. We exclude the two devices deviated from the ideal disk curve (two thinner devices with diameter of ~5.2 μm) along with devices with nonideal geometry (see Figure S5 in SI) for extracting E_Y. Using eq 2 and the measured fundamental mode resonances of the rest devices, we extract an average Young's modulus, $E_Y \approx 261$ GPa, for the β-Ga_2O_3 nanoflakes.

By applying the measured Young's modulus to the resonator model, we complete the frequency scaling of β-Ga_2O_3 nanomechanical resonators from the membrane regime to the disk regime (Figure 3). The plots confirm that all the resonators with ~3.2 μm diameter lie in the disk regime. For the resonators with ~5.2 μm diameter, the thicker two devices lie in the disk regime while the other two resonators lie in the transition regime.

To gain comprehensive understanding of the mechanical properties and resonance performance of the β-Ga_2O_3 diaphragms, we further investigate the multimode resonances and spatial mapping of their mode shapes. Figure 4 displays the measured results from a resonator with a diameter $d \approx 5.7$ μm and thickness $t \approx 23$ nm, which, according to frequency scaling, lies in the transition regime. We measure up to the sixth undriven thermomechanical resonance mode, including resonance spectra and mapping of mode shapes, both before and after annealing. By vividly discerning and visualizing the multimode shapes, we can easily compare and match the resonance modes before and after annealing. Similar to the fundamental-mode resonances, the higher order modes also exhibit clear upshifts in *f*s and enhancement of *Q*s after annealing. The rich resonance modes indicate that this device can potentially be used as the platform for studying the parametric pumping and modes coupling of β-Ga_2O_3 nanomechanical resonators.[44,45]

Importantly, the multimode spatial mapping reveals mechanical properties and features that could be otherwise not visible or measurable, thus shedding more light on understanding these circular drumhead resonators. As shown in Figure 3c, the multimode device measured in Figure 4 ($d \approx 5.7$ μm, $t \approx 23$ nm) behaves in the transition regime, where both built-in tension and flexural rigidity are important in determining its resonance frequencies. When we apply a uniform built-in tension and sweep this tension value in FEM simulations, it yields a uniform stress of $\sigma = 70$ MPa (1.61 N m^{-1} surface tension) that matches the fundamental-mode resonance frequency, whereas the simulated frequencies of higher order modes include well-known degenerate mode pairs that have theoretically identical, nondistinguishable frequencies (i.e., see modes 2 and 3, modes 4 and 5 in the bottom row of Figure 5). In clear contrast, measured resonances labeled with vertical dashed lines in Figure 5 show salient splitting in the degenerate mode pairs, indicating clear broken symmetry. This suggests that the built-in tension cannot be uniform but is anisotropic instead. Such an in-plane anisotropy is also strongly suggested by the spatially mapped multimode shapes demonstrated in the top row of Figure 5, where the nodal lines in the mapped shapes of modes 2 and 3 indicate the stiffer and softer axis of in-plane anisotropy, respectively. To be quantitative, we sweep the anisotropic, biaxial built-in tension in modeling. We find that when the biaxial built-in tensions are 105 and 35 MPa (corresponding to 2.42 N m^{-1} and 0.81 N m^{-1} of surface tension, respectively), the simulated resonances are in good

DOI: 10.1021/acsami.7b13930
ACS Appl. Mater. Interfaces 2017, 9, 43090−43097

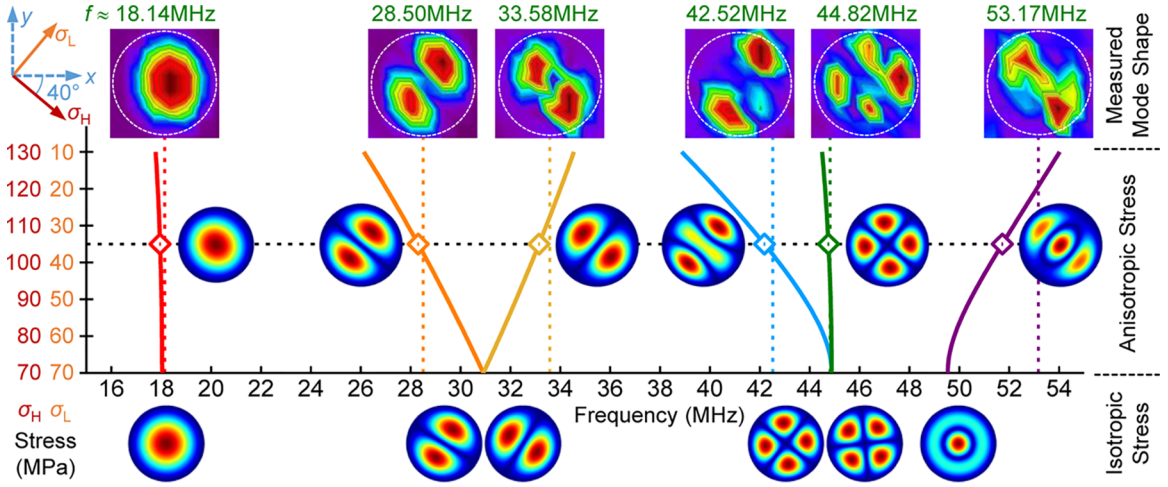

Figure 5. Determination of anisotropic tension in the circular β-Ga_2O_3 diaphragm nanoresonator in Figure 4 by matching the simulated mode shapes and frequencies with the spatially resolved and visualized multimode resonances. The simulation is started using the resonator model with isotropic stress σ = 70 MPa (γ = 1.61 N m^{-1}, last row of the figure). By separating the stress in different directions in simulation, the results with biaxial stress of σ_H = 105 MPa (γ_H = 2.42 N m^{-1}) and σ_L = 35 MPa (γ_L = 0.81 N m^{-1}) best match the measured results, where σ_H direction is 40° off from the horizontal direction.

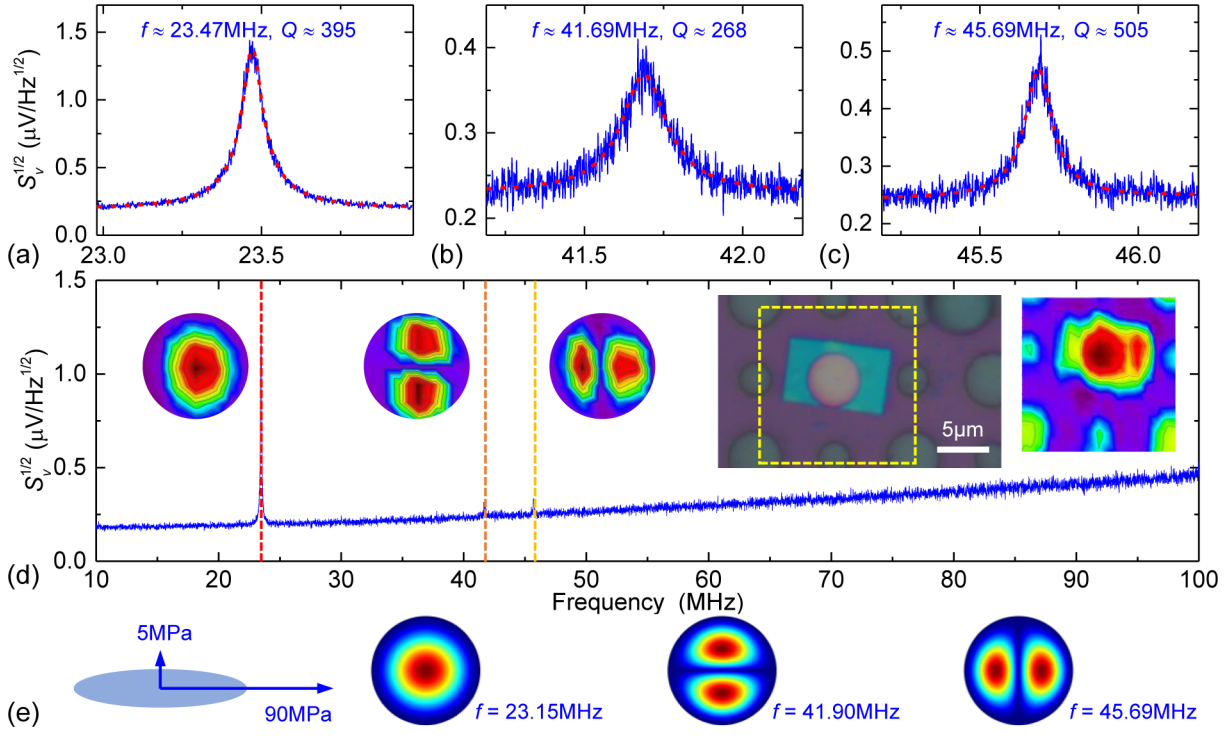

Figure 6. Resonances of a 42 nm thick β-Ga_2O_3 nanomechanical resonator. Zoomed-in measured resonance spectra of (a) first, (b) second, and (c) third resonance mode, and resonance frequencies and quality factors are labeled. (d) Wide-range (10−100 MHz) spectrum of this device with the thermomechanical motion maps of each resonance mode shape visualized by laser interferometry scanning spectromicroscopy. Insets: optical microscopy image of the device with the corresponding static interferometry map. (e) Simulated mode shapes for the device with anisotropic built-in stress.

agreement with the measured multimode responses, for both the frequencies and the mode shapes. We further increase the stress in both directions in simulation to minimize the discrepancy between the simulated resonance frequencies and measured ones. A set of slightly increased biaxial stress, σ_H = 107.5 MPa (γ_H = 2.47 N m^{-1}) and σ_L = 37.5 MPa (γ_L = 0.86 N m^{-1}), generates simulation results (f_1 = 18.18 MHz, f_2 = 28.68 MHz, f_3 = 33.47 MHz, f_4 = 42.77 MHz, f_5 = 45.30 MHz, f_6 = 52.28 MHz) that match excellently with the measured resonance frequencies (f_1 = 18.14 MHz, f_2 = 28.50 MHz, f_3 = 33.58 MHz, f_4 = 42.52 MHz, f_5 = 44.82 MHz, f_6 = 53.17 MHz).

In another thicker, transition regime device ($t \approx$ 42 nm, $d \approx$ 5.2 μm) with three measured resonance modes, multimode resonances with spatial mapping exhibit similar mode-splitting features that reveal in-plane anisotropy in elastic behavior (Figure 6). Once again, parametric sweeping modeling yields an anisotropic built-in tension (5 MPa and 90 MPa, corresponding to 0.21 N m^{-1} and 3.78 N m^{-1} of surface tension) that excellently

DOI: 10.1021/acsami.7b13930
ACS Appl. Mater. Interfaces 2017, 9, 43090−43097

reproduces the measured mode splitting features. These newly resolved nonuniform, anisotropic components of built-in tension in these devices are very reasonable and intuitively understandable, as they can be likely introduced during the nanoflake dry-transfer process where the axis, along which the polymeric tape is pressed down to make contact to substrate and is then lifted up, is likely to build a higher stress component than along its perpendicular direction.

In conclusion, we have demonstrated a new type of UWBG nanomechanical resonator based on synthesized single-crystal β-Ga_2O_3 nanoflakes. These β-Ga_2O_3 nanoresonators demonstrate robust multimode resonances in the high frequency (HF) and very high frequency (VHF) bands ranging from 18 to 75 MHz. From devices operating in the disk regime, the measured resonances determine a Young's modulus of $E_Y \approx 261$ GPa. Multimode spatial mapping discloses new mode splitting features, which in combination with parametric modeling, reveal anisotropic built-in tension (at the levels of 0.2−3.8 N m^{-1}) in devices that operate in the transition regime. Not only does this show that nanomechanical resonances with multimode spatial mapping are a powerful probe for revealing device properties that are otherwise invisible or unmeasurable, but also it helps pave the way for future nanomechanical engineering of β-Ga_2O_3 crystals toward electromechanical and opto-electromechanical devices that harness the crystal's unique properties, which will greatly supplement the rapidly emerging β-Ga_2O_3 electronic devices.

METHODS

β-Ga_2O_3 Nanoflake LPCVD Synthesis. The construction of β-Ga_2O_3 drumhead resonators starts with the synthesis of low-dimensional β-Ga_2O_3 nanoflakes by using a low-pressure chemical vapor deposition (LPCVD) method.[34] The nanoflakes are synthesized on a 3C-SiC epilayer on a Si substrate in a conventional tube furnace with programmable gas and temperature controllers. Over a 1.5 h period at a growth temperature of 950 °C, using high purity Ga pellets (Alfa Aesar, 99.99999%) as source material and O_2 as a gaseous precursor, the formation of β-Ga_2O_3 proceeds, step by step, from β-Ga_2O_3 nanocrystals to β-Ga_2O_3 nanorods and then to nanoflakes, without any foreign catalyst (Figure S1 in SI). The as-grown nanoflakes have widths of ∼2−30 μm and thicknesses of ∼20−140 nm.

Suspended Diaphragm Fabrication. Large arrays of microtrenches are lithographically defined and fabricated on a 290 nm SiO_2-on-Si substrate. The SiO_2 layer is patterned with circular microtrenches using photolithography and then is etched by reactive ion etching (RIE). The depth of resulting SiO_2 microtrenches is 290 nm in this experiment, and the designed nominal values for the microtrench diameters are 3 and 5 μm (corresponding to actual diameters of ∼3.2 μm and ∼5.2 μm measured after the fabrication process).

Using the synthesized β-Ga_2O_3 nanoflakes, we fabricate suspended β-Ga_2O_3 nanostructures by employing an all-dry transfer technique (Figure S2 in SI). With the assistance of thermal release tape, we pick up the β-Ga_2O_3 nanoflakes from the as-grown samples and thermally release the flakes onto the prefabricated 290 nm SiO_2-on-Si substrate with predefined circular microtrenches. Using this method, we fabricate β-Ga_2O_3 circular drumhead resonators with thicknesses of ∼20 to ∼80 nm and diameters of ∼3.2 μm and ∼5.2 μm.

Atomic Force Microscopy (AFM) and Raman Spectroscopy. AFM measurements are conducted with an Agilent 5500 AFM using tapping mode. Raman measurements are performed using a customized micro-Raman system that is integrated into the scanning laser interferometric resonance measurement system (Figure 1d). A 532 nm laser is focused on the transferred β-Ga_2O_3 flake using a 50× microscope objective. The typical laser spot size is ∼1 μm. Raman scattered light from the sample is collected in backscattering geometry and then is guided to a spectrometer (Horiba iHR550) with a 2400 g mm^{-1} grating and 2 min integration time. The Raman signal is recorded using a liquid-nitrogen-cooled charge-coupled device (CCD). The spectral resolution of our system is ∼1 cm^{-1}.

Scanning Laser Interferometry and Spectromicroscopy. Resonances of the circular β-Ga_2O_3 drumhead resonators are characterized using scanning laser interferometry detection techniques (Figure 1d). A 633 nm He−Ne laser is focused on the device surface for detection of the motion-modulated interference between multiple reflections from the vacuum−flake, flake−cavity, and cavity−Si interfaces, which is read out by a low-noise photodetector. A spectrum analyzer is used to measure the signal from the photodetector. We apply an incident laser power of ∼2.8 mW to the devices which are preserved under moderate vacuum conditions (∼20 mTorr) to ensure reasonable signal-to-noise ratio while avoiding overheating. For a given resonance mode, performing the scanning spectromicroscopy measurements yields the spatial mapping and visualization of the mode shape of this resonance. All the interferometry measurements in this work are done at room temperature.

Displacement Sensitivity. We calculate the resonator thermomechanical noise in the displacement domain using

$$S_{x,\mathrm{th}}^{1/2}(\omega) = \left(\frac{4k_B T\omega_m}{M_{m,\mathrm{eff}} \cdot Q_m} \cdot \frac{1}{(\omega^2 - \omega_m^2)^2 + (\omega\omega_m/Q_m)^2} \right)^{1/2} \quad (3)$$

When the device is on resonance ($\omega = \omega_m$), the expression simplifies to

$$S_{x,\mathrm{th}}^{1/2}(\omega_m) = \left(\frac{4k_B T Q_m}{M_{m,\mathrm{eff}} \cdot \omega_m^3} \right)^{1/2} \quad (4)$$

where ω_m, k_B, T, Q_m, and $M_{m,\mathrm{eff}}$ are angular resonance frequency, Boltzmann's constant, temperature, quality factor, and effective mass, respectively, and m denotes the mth mode of the resonator. Effective mass can be calculated using

$$M_{m,\mathrm{eff}} = \frac{\iint_S z_m^2(x, y)\mathrm{d}S}{\pi a^2 \cdot z_{m,\max}^2} M \quad (5)$$

where $z_m(x, y)$ is the mode shape of the mth mode, $z_{m,\max}$ is the maximum displacement, and M is the mass of the resonator. We assume that laser heating is minimal because of the UWBG nature of β-Ga_2O_3, and therefore, the temperature of the sample remains at room temperature ($T \approx 300$ K). The effective mass of the resonator in the disk regime is $M_{\mathrm{eff}} = 0.1828M$. The effective masses of the transition-regime devices are calculated by incorporating FEM simulated mode shapes into eq 5.

Using this analysis, the displacement spectral density of the resonator can be calculated. Hence, we determine the responsivity of the laser interferometry system $\mathcal{R} \equiv S_{v,\mathrm{th}}^{1/2}/S_{x,\mathrm{th}}^{1/2}$ and system sensitivity $S_{x,\mathrm{sys}}^{1/2} \equiv S_{v,\mathrm{sys}}^{1/2}/\mathcal{R}$ for each device. Here, $S_{v,\mathrm{th}}^{1/2}$ and $S_{v,\mathrm{sys}}^{1/2}$ are the voltage domain thermomechanical noise and the noise level of the measurement system, respectively. For all devices in this work, the responsivities and sensitivities of the interferometry system range from 12 μV pm^{-1} to 60 μV pm^{-1} and from 4 fm $Hz^{-1/2}$ to 19 fm $Hz^{-1/2}$, respectively.

ASSOCIATED CONTENT

Supporting Information

The Supporting Information is available free of charge on the ACS Publications website at DOI: 10.1021/acsami.7b13930.

Material synthesis and resonator fabrication processes; Raman spectroscopy for crystal quality characterization; optical interferometry displacement sensitivity analysis; Young's modulus extraction and resonator frequency scaling; summary of devices and their measured parameters

(PDF)

DOI: 10.1021/acsami.7b13930
ACS Appl. Mater. Interfaces 2017, 9, 43090−43097

AUTHOR INFORMATION

Corresponding Author

*E-mail: philip.feng@case.edu.

ORCID

Xu-Qian Zheng: 0000-0003-4705-771X

Philip X.-L. Feng: 0000-0002-1083-2391

Notes

The authors declare no competing financial interest.

ACKNOWLEDGMENTS

We thank financial support from the U.S. Department of Energy (DOE) EERE Grant (DE-EE0006719) and the Great Lakes Energy Institute (GLEI) ThinkEnergy Fellowship. C. A. Zorman and P. X-L. Feng thank financial support from the National Science Foundation (NSF) SNM Program (Grant CMMI-1246715). S. Rafique and H. Zhao thank financial support from the NSF DMR Grant (1755479). L. Han and H. Zhao thank financial support from the NSF CNS Grant (1664368). We thank J. P. McCandless for helpful discussions. Part of the device fabrication was performed at the Cornell NanoScale Science and Technology Facility (CNF), a member of the National Nanotechnology Infrastructure Network (NNIN), supported by the National Science Foundation (Grant ECCS-0335765).

REFERENCES

(1) Kimoto, T.; Cooper, J. A. *Fundamentals of Silicon Carbide Technology: Growth, Characterization, Devices, and Applications*; John Wiley & Sons: Singapore, 2014.

(2) Hudgins, J. L.; Simin, G. S.; Santi, E.; Khan, M. A. An Assessment of Wide Bandgap Semiconductors for Power Devices. *IEEE Trans. Power Electron.* **2003**, *18*, 907−914.

(3) Xi, Y.; Schubert, E. F. Junction−Temperature Measurement in GaN Ultraviolet Light-Emitting Diodes using Diode Forward Voltage Method. *Appl. Phys. Lett.* **2004**, *85*, 2163−2165.

(4) Li, D.; Sun, X.; Song, H.; Li, Z.; Chen, Y.; Jiang, H.; Miao, G. Realization of a High-Performance GaN UV Detector by Nanoplasmonic Enhancement. *Adv. Mater.* **2012**, *24*, 845−849.

(5) Yan, F.; Xin, X.; Aslam, S.; Zhao, Y.; Franz, D.; Zhao, J. H.; Weiner, M. 4H-SiC UV Photo Detectors with Large Area and Very High Specific Detectivity. *IEEE J. Quantum Electron.* **2004**, *40*, 1315−1320.

(6) Cimalla, V.; Pezoldt, J.; Ambacher, O. Group III Nitride and SiC Based MEMS and NEMS: Materials Properties, Technology and Applications. *J. Phys. D: Appl. Phys.* **2007**, *40*, 6386−6434.

(7) Feng, X. L.; White, C. J.; Hajimiri, A.; Roukes, M. L. A Self-Sustaining Ultrahigh-Frequency Nanoelectromechanical Oscillator. *Nat. Nanotechnol.* **2008**, *3*, 342−346.

(8) Feng, X. L.; Matheny, M. H.; Zorman, C. A.; Mehregany, M.; Roukes, M. L. Low Voltage Nanoelectromechanical Switches Based on Silicon Carbide Nanowires. *Nano Lett.* **2010**, *10*, 2891−2896.

(9) Nam, C.-Y.; Jaroenapibal, P.; Tham, D.; Luzzi, D. E.; Evoy, S.; Fischer, J. E. Diameter-Dependent Electromechanical Properties of GaN Nanowires. *Nano Lett.* **2006**, *6*, 153−158.

(10) Lorenz, M. R.; Woods, J. F.; Gambino, R. J. Some Electrical Properties of the Semiconductor β-Ga_2O_3. *J. Phys. Chem. Solids* **1967**, *28*, 403−404.

(11) Ueda, N.; Hosono, H.; Waseda, R.; Kawazoe, H. Anisotropy of Electrical and Optical Properties in β-Ga_2O_3 Single Crystals. *Appl. Phys. Lett.* **1997**, *71*, 933−935.

(12) Oishi, T.; Koga, Y.; Harada, K.; Kasu, M. High-Mobility β-Ga_2O_3 (201) Single Crystals Grown by Edge-Defined Film-Fed Growth Method and Their Schottky Barrier Diodes with Ni Contact. *Appl. Phys. Express* **2015**, *8*, 031101.

(13) Higashiwaki, M.; Sasaki, K.; Kuramata, A.; Masui, T.; Yamakoshi, S. Gallium Oxide (Ga_2O_3) Metal-Semiconductor Field-Effect Transistors on Single-Crystal β-Ga_2O_3 (010) Substrates. *Appl. Phys. Lett.* **2012**, *100*, 013504.

(14) Ma, N.; Tanen, N.; Verma, A.; Guo, Z.; Luo, T.; Xing, H. G.; Jena, D. Intrinsic Electron Mobility Limits in β-Ga_2O_3. *Appl. Phys. Lett.* **2016**, *109*, 212101.

(15) Green, A. J.; Chabak, K. D.; Heller, E. R.; Fitch, R. C.; Baldini, M.; Fiedler, A.; Irmscher, K.; Wagner, G.; Galazka, Z.; Tetlak, S. E.; Crespo, A.; Leedy, K.; Jessen, G. H. 3.8-MV/cm Breakdown Strength of MOVPE-Grown Sn-Doped β-Ga_2O_3 MOSFETs. *IEEE Electron Device Lett.* **2016**, *37*, 902−905.

(16) Chabak, K. D.; Moser, N.; Green, A. J.; Walker, D. E., Jr.; Tetlak, S. E.; Heller, E.; Crespo, A.; Fitch, R.; McCandless, J. P.; Leedy, K.; Baldini, M.; Wagner, G.; Galazka, Z.; Li, X.; Jessen, G. Enhancement-Mode Ga_2O_3 Wrap-Gate Fin Field-Effect Transistors on Native (100) β-Ga_2O_3 Substrate with High Breakdown Voltage. *Appl. Phys. Lett.* **2016**, *109*, 213501.

(17) Higashiwaki, M.; Sasaki, K.; Murakami, H.; Kumagai, Y.; Koukitu, A.; Kuramata, A.; Masui, T.; Yamakoshi, S. Recent Progress in Ga_2O_3 Power Electronics. *Semicond. Sci. Technol.* **2016**, *31*, 034001.

(18) Zhou, H.; Si, M.; Alghamdi, S.; Qiu, G.; Yang, L.; Ye, P. D. High-Performance Depletion/Enhancement-Mode β-Ga_2O_3 on Insulator (GOOI) Field-Effect Transistors with Record Drain Currents of 600/450 mA/mm. *IEEE Electron Device Lett.* **2017**, *38*, 103−106.

(19) Yu, M.-F.; Atashbar, M. Z.; Chen, X. Mechanical and Electrical Characterization of β-Ga_2O_3 Nanostructures for Sensing Applications. *IEEE Sens. J.* **2005**, *5*, 20−25.

(20) Nikolaev, V. I.; Maslov, V.; Stepanov, S. I.; Pechnikov, A. I.; Krymov, V.; Nikitina, I. P.; Guzilova, L. I.; Bougrov, V. E.; Romanov, A. E. Growth and Characterization of β-Ga_2O_3 Crystals. *J. Cryst. Growth* **2017**, *457*, 132−136.

(21) Zou, R.; Zhang, Z.; Liu, Q.; Hu, J.; Sang, L.; Liao, M.; Zhang, W. High Detectivity Solar-Blind High-Temperature Deep-Ultraviolet Photodetector Based on Multi-Layered (l00) Facet-Oriented β-Ga_2O_3 Nanobelts. *Small* **2014**, *10*, 1848−1856.

(22) Kong, W.-Y.; Wu, G.-A.; Wang, K.-Y.; Zhang, T.-F.; Zou, Y.-F.; Wang, D.-D.; Luo, L.-B. Graphene- β-Ga_2O_3 Heterojunction for Highly Sensitive Deep UV Photodetector Application. *Adv. Mater.* **2016**, *28*, 10725−10731.

(23) Jangir, R.; Porwal, S.; Tiwari, P.; Mondal, P.; Rai, S. K.; Ganguli, T.; Oak, S. M.; Deb, S. K. Photoluminescence Study of β-Ga_2O_3 Nanostructures Annealed in Different Environments. *J. Appl. Phys.* **2012**, *112*, 034307.

(24) Tomm, Y.; Reiche, P.; Klimm, D.; Fukuda, T. Czochralski Grown Ga_2O_3 Crystals. *J. Cryst. Growth* **2000**, *220*, 510−514.

(25) Galazka, Z.; Uecker, R.; Irmscher, K.; Albrecht, M.; Klimm, D.; Pietsch, M.; Brützam, M.; Bertram, R.; Ganschow, S.; Fornari, R. Czochralski Growth and Characterization of Beta-Ga_2O_3 Single Crystals. *Cryst. Res. Technol.* **2010**, *45*, 1229−1236.

(26) Ueda, N.; Hosono, H.; Waseda, R.; Kawazoe, H. Synthesis and Control of Conductivity of Ultraviolet Transmitting Beta-Ga_2O_3 Single Crystals. *Appl. Phys. Lett.* **1997**, *70*, 3561−3563.

(27) Tomm, Y.; Ko, J. M.; Yoshikawa, A.; Fukuda, T. Floating Zone Growth of β-Ga_2O_3: a New Window Material for Optoelectronic Device Applications. *Sol. Energy Mater. Sol. Cells* **2001**, *66*, 369−374.

(28) Villora, E. G.; Shimamura, K.; Yoshikawa, Y.; Aoki, K.; Ichinose, N. Large-Size β-Ga_2O_3 Single Crystals and Wafers. *J. Cryst. Growth* **2004**, *270*, 420−426.

(29) Kuramata, A.; Koshi, K.; Watanabe, S.; Yamaoka, Y.; Masui, T.; Yamakoshi, S. High-Quality β-Ga_2O_3 Single Crystals Grown by Edge-Defined Film-Fed Growth. *Jpn. J. Appl. Phys.* **2016**, *55*, 1202A2.

(30) Kumar, S.; Sarau, G.; Tessarek, C.; Bashouti, M. Y.; Hähnel, A.; Christiansen, S.; Singh, R. Study of Iron-Catalysed Growth of β-Ga_2O_3 Nanowires and Their Detailed Characterization using TEM, Raman and Cathodoluminescence Techniques. *J. Phys. D: Appl. Phys.* **2014**, *47*, 435101.

DOI: 10.1021/acsami.7b13930
ACS Appl. Mater. Interfaces 2017, 9, 43090−43097

(31) Zhang, J.; Jiang, F.; Yang, Y.; Li, J. Catalyst-Assisted Vapor-Liquid-Solid Growth of Single-Crystal Ga_2O_3 Nanobelts. *J. Phys. Chem. B* **2005**, *109*, 13143−13147.
(32) Rafique, S.; Han, L.; Zorman, C. A.; Zhao, H. Synthesis of Wide Bandgap β-Ga_2O_3 Rods on 3C-SiC-on-Si. *Cryst. Growth Des.* **2016**, *16*, 511−517.
(33) Ohira, S.; Sugawara, T.; Nakajima, K.; Shishido, T. Synthesis and Structural Investigation of β-Ga_2O_3 Nanosheets and Nanobelts. *J. Alloys Compd.* **2005**, *402*, 204−207.
(34) Rafique, S.; Han, L.; Lee, J.; Zheng, X.-Q.; Zorman, C. A.; Feng, P. X.-L.; Zhao, H. Synthesis and Characterization of Ga_2O_3 Nanosheets on 3C-SiC-on-Si by Low Pressure Chemical Vapor Deposition. *J. Vac. Sci. Technol., B: Nanotechnol. Microelectron.: Mater., Process., Meas., Phenom.* **2017**, *35*, 011208.
(35) Rafique, S.; Han, L.; Tadjer, M. J.; Freitas, J. A., Jr.; Mahadik, N. A.; Zhao, H. Homoepitaxial Growth of β-Ga_2O_3 Thin Films by Low Pressure Chemical Vapor Deposition. *Appl. Phys. Lett.* **2016**, *108*, 182105.
(36) Rafique, S.; Han, L.; Neal, A. T.; Mou, S.; Tadjer, M. J.; French, R. H.; Zhao, H. Heteroepitaxy of N-type β-Ga_2O_3 Thin Films on Sapphire Substrate by Low Pressure Chemical Vapor Deposition. *Appl. Phys. Lett.* **2017**, *109*, 132103.
(37) Yoshioka, S.; Hayashi, H.; Kuwabara, A.; Oba, F.; Matsunaga, K.; Tanaka, I. Structures and Energetics of Ga_2O_3 Polymorphs. *J. Phys.: Condens. Matter* **2007**, *19*, 346211.
(38) Kranert, C.; Sturm, C.; Schmidt-Grund, R.; Grundmann, M. Raman Tensor Elements of β-Ga_2O_3. *Sci. Rep.* **2016**, *6*, 35964.
(39) Wang, Z.; Lee, J.; Feng, P. X.-L. Spatial Mapping of Multimode Brownian Motions in High-Frequency Silicon Carbide Microdisk Resonators. *Nat. Commun.* **2014**, *5*, 5158.
(40) Lee, J.; Krupcale, M. J.; Feng, P. X.-L. Effects of γ-Ray Radiation on Two-Dimensional Molybdenum Disulfide (MoS_2) Nanomechanical Resonators. *Appl. Phys. Lett.* **2016**, *108*, 023106.
(41) Zheng, X.-Q.; Lee, J.; Feng, P. X.-L. Hexagonal Boron Nitride (h-BN) Nanomechanical Resonators with Spatially Visualized Motion. *Microsystems Nanoengineering* **2017**, *3*, 17038.
(42) Suzuki, H.; Yamaguchi, N.; Izumi, H. Theoretical and Experimental Studies on the Resonance Frequencies of a Stretched Circular Plate: Application to Japanese Drum Diaphragms. *Acoust. Sci. Technol.* **2009**, *30*, 348−354.
(43) Lee, J.; Wang, Z.; He, K.; Shan, J.; Feng, P. X.-L. High Frequency MoS_2 Nanomechanical Resonators. *ACS Nano* **2013**, *7*, 6086−6091.
(44) Deng, G.-W.; Zhu, D.; Wang, X.-H.; Zou, C.-L.; Wang, J.-T.; Li, H.-O.; Cao, G.; Liu, D.; Li, Y.; Xiao, M.; Guo, G.-C.; Jiang, K.-L.; Dai, X.-C.; Guo, G.-P. Strongly Coupled Nanotube Electromechanical Resonators. *Nano Lett.* **2016**, *16*, 5456−5462.
(45) Zhu, D.; Wang, X.-H.; Kong, W.-C.; Deng, G.-W.; Wang, J.-T.; Li, H.-O.; Cao, G.; Xiao, M.; Jiang, K.-L.; Dai, X.-C.; Guo, G.-C.; Nori, F.; Guo, G.-P. Coherent Phonon Rabi Oscillations with a High-Frequency Carbon Nanotube Phonon Cavity. *Nano Lett.* **2017**, *17*, 915−921.

NOTE ADDED AFTER ASAP PUBLICATION

This paper was published on the Web on November 27, 2017. Figure 4 was replaced, and the corrected version was reposted on November 28, 2017.

DOI: 10.1021/acsami.7b13930
ACS Appl. Mater. Interfaces 2017, 9, 43090−43097